



Titan's North–South Haze Asymmetry Ratio and Boundary at Visible Wavelengths over the Cassini Mission

Aadvik S. Vashist^{1,2} , Michael F. Heslar¹ , Jason W. Barnes¹ , Corbin Hennen¹, and Ralph D. Lorenz³

¹Department of Physics; University of Idaho; Moscow, ID 83844, USA

²River Hill High School; Clarksville, MD 21029, USA

³Johns Hopkins University Applied Physics Laboratory; Laurel, MD 20723, USA

Received 2023 February 10; revised 2023 June 3; accepted 2023 June 7; published 2023 June 30

Abstract

We document the evolution of the north–south asymmetry (NSA) of Titan's haze albedo during the Cassini mission between 2004 and 2017. We analyze coadded cube images taken at 96 distinct wavelengths between 0.35 and 1.05 μm by the Cassini Visual and Infrared Mapping Spectrometer (VIMS-V) instrument from 14 Titan flybys. Over half of a Titan year, we observe a near-complete transition in the NSA boundary latitude across the geographic equator from the southern to the northern hemisphere, including a 3 yr fading of the boundary for several years after the equinox. The fading transition of the NSA matches previous observations of a reversal of the NSA in Hubble Space Telescope images of Titan before the winter solstice between 1997 and 2000. A comparison of NSA images taken at similar times but different phase angles shows the NSA boundary is detectable, albeit with less contrast, at moderately high phase angles ($\sim 90^\circ$). Analysis of the NSA boundary in T61 and T67 VIMS images further supports a small tilt between the superrotating atmosphere and the solid body of Titan, as suggested in a previous analysis of 0.890 μm images from the Cassini Imaging Science Subsystem.

Unified Astronomy Thesaurus concepts: [Astronomy data modeling \(1859\)](#); [Astronomy image processing \(2306\)](#); [Titan \(2186\)](#); [Atmospheric evolution \(2301\)](#); [Atmospheric dynamics \(2300\)](#); [Albedo \(2321\)](#); [Computational astronomy \(293\)](#)

1. Introduction

Saturn's moon Titan exhibits many properties not found in other satellites. As first observed by Voyager 1 (Smith et al. 1981), Titan's ubiquitous atmospheric haze prevents optical imaging of the surface. The haze distribution varies as a function of latitude (Sromovsky et al. 1981), altitude (Smith et al. 1982; Tomasko et al. 2005), and time (Lorenz et al. 1997; West et al. 2011). Titan's haze also shows albedo differences between its northern and southern hemispheres that shift near the equator. As the seasons progress, atmospheric circulation changes the global haze distribution, culminating in a reversal every 15 yr (Brown et al. 2009). The reversal presents as an albedo dichotomy in the otherwise featureless atmosphere. The existence of the asymmetry also results in a distinct boundary line that separates the northern and southern hemispheres.

The Voyager 1 flyby highlighted the existence of a north–south asymmetry (NSA) between the two hemispheres (Smith et al. 1981), which we show in Figure 1. Previous discoveries also found a tilt of the boundary line relative to the solid-body equator of Titan (Roman et al. 2009). The boundary, as reported by Sromovsky et al. (1981) with Voyager 1 data, was located at roughly 5.5°S . More recent discoveries show a seasonal reversal in the latitude of the asymmetry across the equator.

The movement of the NSA boundary reveals essential details of the global atmospheric properties and circulation patterns of Titan (Hirtzig et al. 2006). Titan disk observations from flyby missions and professional telescopes provide sporadic temporal

and wavelength coverage of the NSA, leading to incomplete records on haze circulation with large errors (Lorenz et al. 2001, 2004). In addition, previous studies often use special case methodologies, where results are tied to their data sets to calculate and subsequently compare those previous NSA boundary latitudes (Roman et al. 2009).

More recent studies have the temporal coverage to study detailed aspects for a substantial portion of the NSA cycle with individual data sets. Karkoschka (2022) modeled NSA reversal at different altitudes with the Hubble Space Telescope (HST) Space Telescope Imaging Spectrograph image cubes. Kutsop et al. (2022) completed an analysis of circumglobal haze bands in a variety of Cassini imagery data sets.

In this paper, we document on the seasonal changes in Titan's lower atmospheric haze near the equator using Cassini observations of visible wavelengths for the purpose of comparison with previous studies. The observations of seasonal haze changes through visible wavelengths allow us to extend the temporal baseline of previous observations and to track one seasonal cycle coherently with a single uniform data set. The Cassini Visual and Infrared Mapping Spectrometer instrument (VIMS) collected spectral maps at 96 visible and near-infrared wavelengths between 0.35 and 1.05 μm , which predominantly sampled the stratosphere ($\sim 70\text{--}120\text{ km}$).

Section 2 describes how we modify the main NSA image analysis algorithm from Roman et al. (2009) with considerations for the VIMS data characteristics. In Section 3, We determine the latitude of the asymmetry at 76 of the 96 distinct wavelengths, excluding atmospheric windows where the visible surface precludes haze measurements (Vixie et al. 2012). Each distinct wavelength accesses a different altitude because of the varying atmospheric opacity. In Section 4, we locate the latitude of the NSA boundary on 13 distinct flybys.



Original content from this work may be used under the terms of the [Creative Commons Attribution 4.0 licence](#). Any further distribution of this work must maintain attribution to the author(s) and the title of the work, journal citation and DOI.

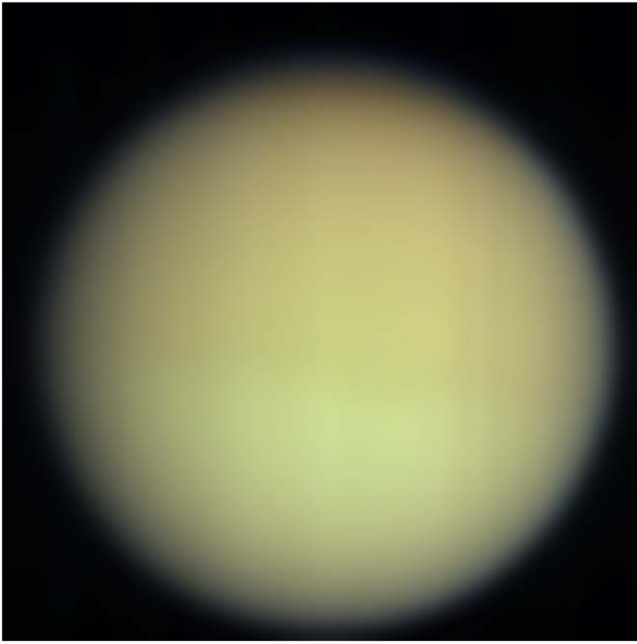


Figure 1. A T62 image of VIMS cube CM_1634082284_1 taken on 2009 October 12 shows a typical low-phase-angle view of Titan with the NSA at visible wavelengths from the VIMS instrument (VIMS-V). The colors are an approximation of true color using the VIMS-V channels. The overall orange color comes from the spectral and scattering properties of the haze particles as well as atmospheric absorption and Rayleigh scattering, which predominate at bluer wavelengths. North is upwards in the image.

We also determine the albedo contrast between the northern and southern hemispheres with regard to wavelength to calculate the boundary latitude, north–south (NS) flux ratios, and the tilt angle of the asymmetry. Finally, in Section 5, we compare our results to the existing archive of NSA boundary observations and discuss the implications of these findings on the atmospheric conditions of Titan.

2. Observations and Methods

As shown in Table 1, we analyze Cassini VIMS observations of Titan from 12 targeted flybys from 2004 to 2015 and two nontargeted flybys taken in 2017. Each flyby observed Titan from 0.356 to 1.046 μm in 96 distinct wavelength channels to sample the transition from southern summer to northern summer (Brown et al. 2004). We selected these particular flybys based on boundary visibility, sufficient time cadence, and baseline so as to obtain measurements spaced out over the entire period of Cassini observations. For a majority of the flybys, the spatial sampling per pixel is ~ 45 km or 1° of latitude. For the NSA, one hemisphere appears brighter and the other dimmer, with a semidistinct line near the tropics (i.e., low latitudes) dividing the two. The identification of the brighter hemisphere depends on the season and the observed wavelength that samples at the different altitudes as shown in Figure 2. Lorenz et al. (1997) attribute the reversal to the separately varying single-scattering albedo of the haze and gas as a function of wavelength. At short visible wavelengths (Figure 2, left), the haze has a low albedo, but the gas itself is relatively bright due to Rayleigh scattering. Thus, more haze leads to a darker hemisphere at short wavelengths. At near-infrared wavelengths close to the visible (Figure 2, right), however, the haze single-scattering albedo is high, and methane starts to absorb,

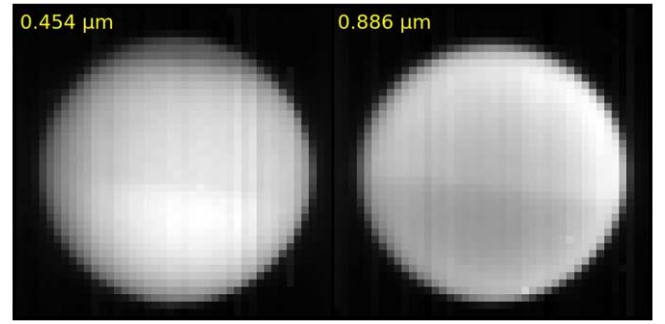


Figure 2. Titan’s NSA is evident in two individual band images from the same VIMS cube in Figure 1 (CM_1634082284_1). In the left cube, the southern hemisphere appears brighter at blue wavelengths. In contrast, the NSA reverses in the right image within a methane absorption band at 0.886 μm . Vertical striping artifacts are present in the images.

making the gas dim. So higher haze concentrations make a hemisphere brighter at long wavelengths. The Cassini VIMS flybys used in this study had varied spacecraft distances, leading to a range of spatial resolutions. We chose these particular flybys as ones where a majority or all of Titan’s disk is observed. Figure 3 outlines our VIMS image processing algorithm. An issue found in the VIMS data is the vertical striping noise in the original images. We could not directly correct the striping noise because the data used to subtract the background on board Cassini were not transmitted back to Earth (Brown et al. 2004). To mitigate the striping issues, we increased the signal-to-noise ratio by coadding images, and then mapping the final coadded image onto a cylindrical projection (Vixie et al. 2012). The spatial sampling of the cylindrical images is ~ 45 km or 1° of latitude. Note that the vertical striping appears as superimposed stripes across cylindrical projections. Additionally, these projections do not include limb pixels with an emission angle above 60° and thus minimize limb-darkening effects. Images at 96 distinct wavelengths, also known as bands, were created for each flyby. After we generate a final set of images, we adapt the methods from Roman et al. (2009) to determine the latitude of the NSA boundary. We shift the images by 6°N and 6°S and then subtract the shifted images from each other to create a high brightness contrast of each image, which highlights the presence of an asymmetry (Roman et al. 2009). These maps were then sequentially analyzed along each longitude using a sixth-order polynomial fit to smooth out signal variations. We found the locations of critical points using the derivative function of the fit; extraneous values, such as imaginary solutions and numbers outside of the latitude range, were removed to leave only the latitude location of the NSA at each longitude column. Our algorithm then finds the latitude value of the NSA transition for all the longitude columns within each projection and then averages them to determine the location of the NSA for each band in the flyby. Since each column has a varied value for the NSA, we applied a moving average to the data to flatten irregularities in the column brightness data. Using the latitude value found in each image, we apply a simple average of the brightness 30°N and 30°S of the NSA transition to determine the NS flux ratio. We derive I/F values using the average visible latitudes, where each latitude is an average of all visible longitudinal brightness values. We can attribute various inaccuracies in our results to sampling area, surface wavelengths, changing subsolar and sub-spacecraft latitudes, image manipulation inaccuracies,

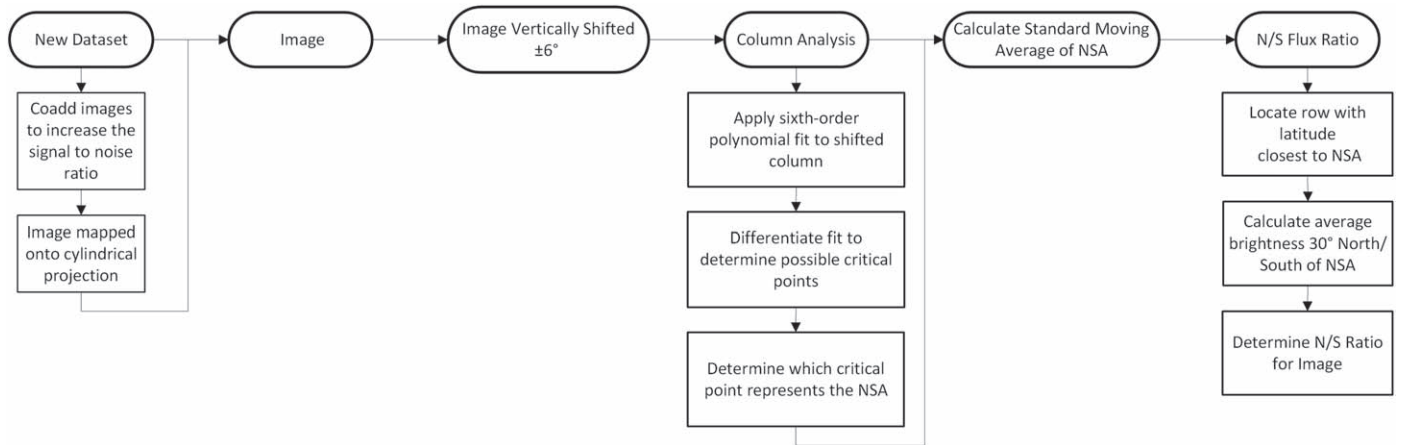


Figure 3. Here we present a flowchart of the image processing procedures to obtain the NSA boundary latitude and the NS flux ratio from an individual VIMS cube image.

Table 1
NS Boundary Observations

Year	Month	Source	Cassini Flyby	λ (μm)	L_s ($^\circ$)	Subsolar Latitude ($^\circ$)	Boundary Latitude ($^\circ$)	Citation
1980	Nov	Voyager/ISS		0.450	8	4	-5.5 ± 1	Squyres et al. (1984)
1981	Aug	Voyager/ISS		0.450	16	8	-5.5 ± 1	Squyres et al. (1984)
1990	Aug	HST/WFPC		0.440	122	23	32 ± 10	Caldwell et al. (1992)
1992	Aug	HST/WFPC		0.440	145	16	20 ± 10	Smith et al. (1992)
1994	Oct	HST/WFPC2		0.440	168	5.8	15 ± 5	Lorenz et al. (1997)
1995	Aug	HST/WFPC2		0.440	177	1.3	15 ± 5	Lorenz et al. (1997)
1997	Nov	HST/WFPC2		0.889	202	-10.7	10 ± 15	Lorenz et al. (1999)
2000	Nov–Dec	HST/WFPC2		0.889	242	-24	...	Lorenz et al. (2001)
2002	Dec	HST/ACS		0.435, 889	271	-26.7	-20 ± 10	Inspection of Lorenz et al. (2006)
2003	Dec	HST/ACS		0.435	288	-25.6	-20 ± 5	Inspection of Lorenz et al. (2006)
2004	Oct	Cassini/VIMS	Ta	0.356–1.046	300	-23.2	-12 ± 3	This work
2004	Oct–Dec	Cassini/ISS		0.889	300	-23	-8 ± 2	Roman et al. (2009)
2005	Feb–Dec	Cassini/ISS		0.889	309	-21	-8 ± 2	Roman et al. (2009)
2005	Oct	Cassini/VIMS	T8	0.356–1.046	314	-19.6	-12 ± 3	This work
2007	May–Dec	Cassini/ISS		0.889	0.335	-11.5	-8 ± 2	Roman et al. (2009)
2007	May	Cassini/VIMS	T31	0.356–1.046	333	-12.0	-12 ± 3	This work
2009	Aug	Cassini/VIMS	T61	0.356–1.046	1	0.4	-12 ± 3	This work
2009	Oct	Cassini/VIMS	T62	0.356–1.046	3	1	-12 ± 3	This work
2010	Apr	Cassini/VIMS	T67	0.356–1.046	8	8	-12 ± 3	This work
2011	Dec	Cassini/VIMS	T79	0.356–1.046	29	13	-10 ± 4	This work
2012	Jul	Cassini/VIMS	T85	0.356–1.046	36	15	-10 ± 4	This work
2013	Oct	Cassini/VIMS	T92	0.356–1.046	47	19	-5 ± 4	This work
2014	May	Cassini/VIMS	T101	0.356–1.046	57	22	...	This work
2015	Jan	Cassini/VIMS	T108	0.356–1.046	64	24	...	This work
2015	Nov	Cassini/VIMS	T114	0.356–1.046	74	26	...	This work
2017	Jun	Cassini/VIMS	278T ¹	0.356–1.046	91	27	10 ± 3	This work
2017	July	Cassini/VIMS	283T ¹	0.356–1.046	92	27	10 ± 4	This work

Note. ACS = Advanced Camera for Surveys.

^a Nontargeted flyby of Titan.

and/or phase angle differences within the flybys. We determine uncertainties in our image processing algorithm through the standard deviation of the derived latitude value of every image. Additionally, instrumental artifacts and noise within the VIMS-V instrument play a factor. Inherent systematic errors also derive from the softness of the boundary itself and any potential offset between the atmospheric pole and the geographic pole.

3. NSA

3.1. Meridional Brightness Profiles

Figure 4 displays various meridional brightness profiles from specific flybys at two wavelengths: one near-infrared and one visible. At certain wavelengths, the location of the boundary generally corresponds with either the maxima or minima of the profiles, depending on the season. The values of

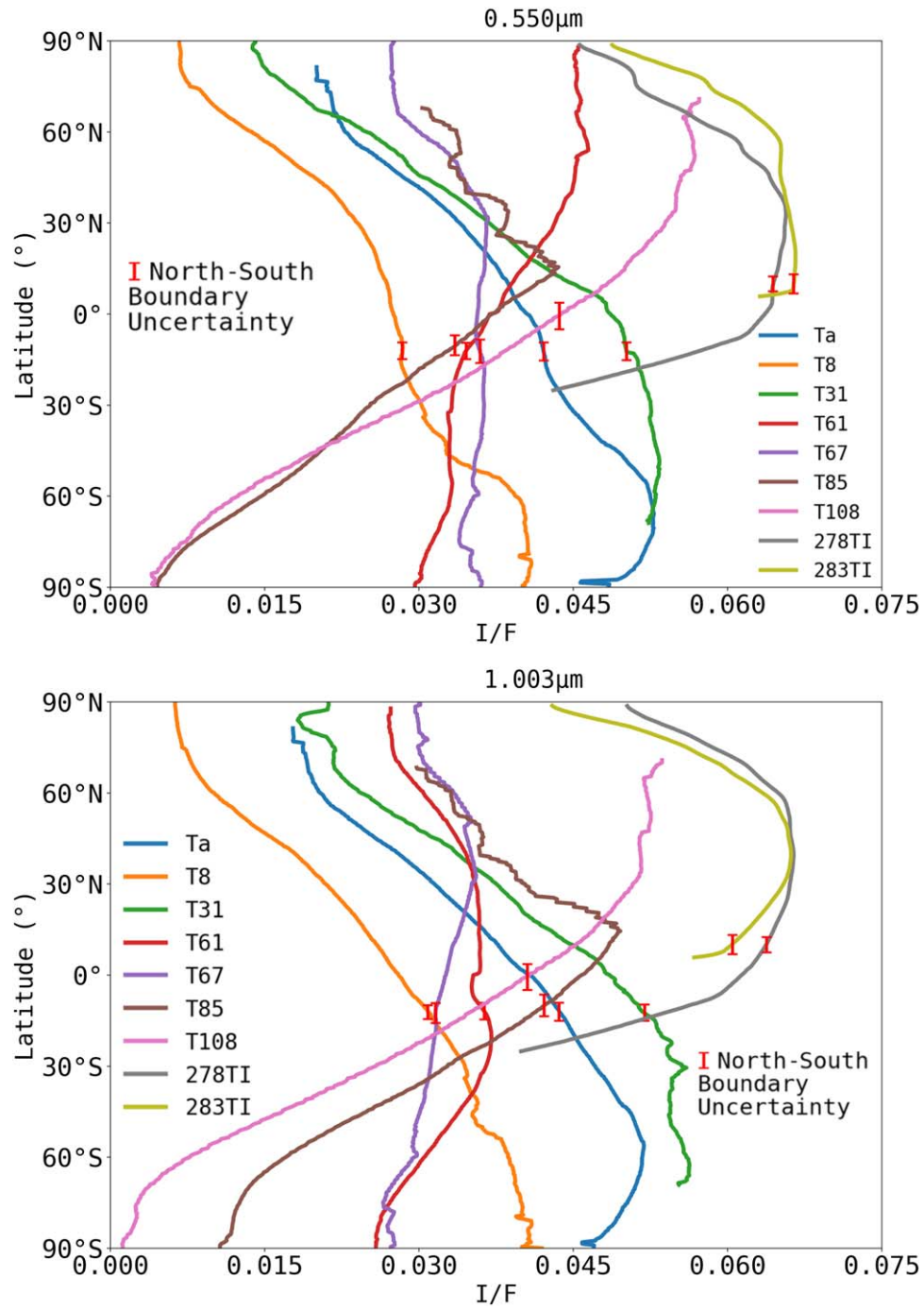


Figure 4. Meridional disk brightness (I/F) profiles across Titan from select Cassini flybys over a Titan half year along with published HST NS ratio spectra in the top panel. The top plot shows the profile at $0.550 \mu\text{m}$ and the bottom at $1.003 \mu\text{m}$. The error bars represent the NS boundary location and its uncertainty for each flyby at that wavelength. The shape and trends of the profile did not exhibit much change between 2004 and 2007 (Ta–T31). With the onset of the vernal equinox in T61, the meridional profile developed dramatic changes resulting from both varying solar illumination and dynamic atmospheric structure, with a near-complete latitudinal reversal by 2017 (278TI). It is important to note that in T85, 278TI, and 283TI, drop-offs are removed as the disks are terminated. Additionally, the coaddition of longitudinal data tends to resolve the NSA boundary poorly, resulting in sometimes indistinct NSA boundary transitions, like in 278TI.

each profile are averaged over longitude to minimize noise from striping and various other artifacts. Flybys from the Prime mission (2004–2008) in southern summer have a single relative maximum that increases in latitude as time progresses, whereas later flybys show greater variance. The movement of the relative extrema also serves to visualize the changes in the NS flux ratio. We note that limited spatial coverage in the VIMS images of the nontargeted flybys (278TI, 283TI) causes

the early cutoff in their NS flux ratio profiles just below the equator in Figure 4.

3.2. NS Flux Ratio Spectra

Figure 5 displays the contrast ratio, a comparison between regions 30° north and south of the NS boundary, as a function of wavelength in four panels. The different lines represent different

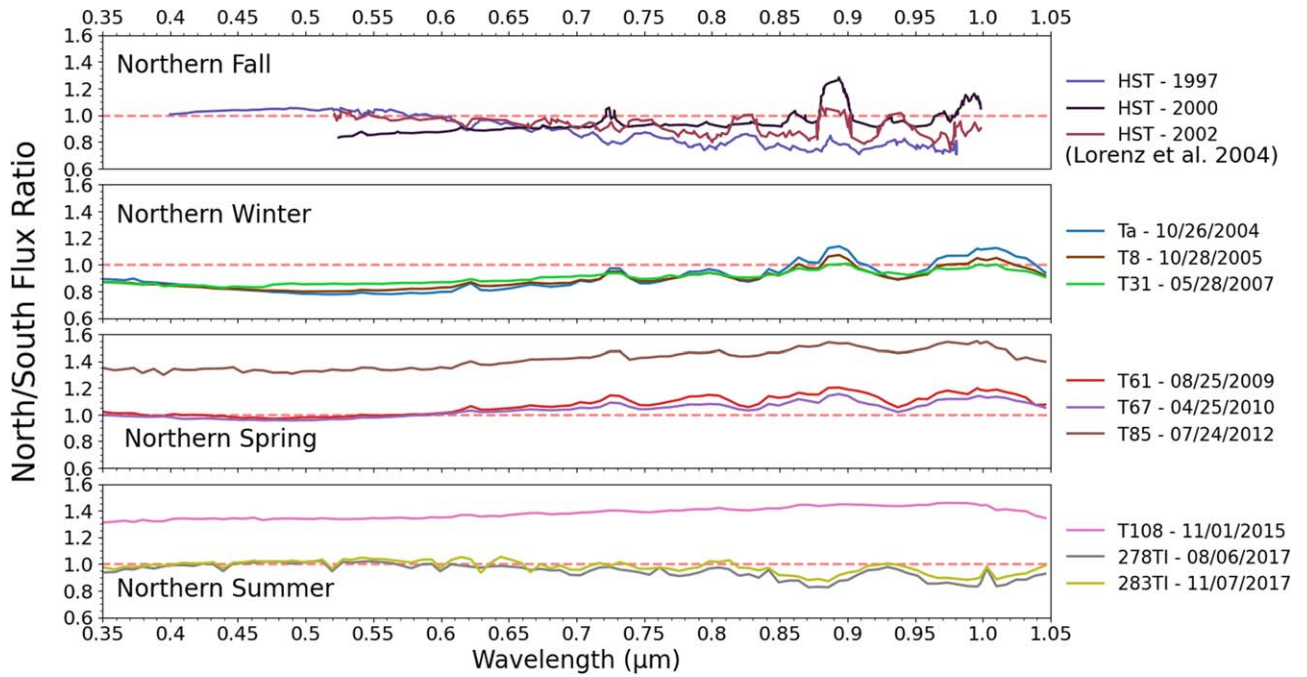


Figure 5. NS flux ratio spectra (average ratio of I/Fs 30° above and below the NSA boundary latitude) from select flybys over a Titan half year. Note that wavelengths where methane absorbs (e.g., $0.89 \mu\text{m}$) tend to show an inverted NS flux ratio relative to methane windows (e.g., $0.93 \mu\text{m}$). The Ta and T8 spectra show distinct features, while the T114 and 278TI spectra show those same features with a flipped concavity. Changing illumination and viewing conditions can shift these NS ratio spectra vertically. Changing illumination cannot, however, invert absorption lines as we see happen from northern winter into northern spring at $0.89 \mu\text{m}$. Thus much of the variation in spectral shape can be attributed to varying atmospheric structure. The other spectra from T31 to T108 that were recorded closer to the vernal equinox show subdued or nonexistent features, indicating a more uniform meridional haze profile for Titan.

flybys, with flybys being sorted into either northern fall, northern winter, equinox, or northern summer. The total observed time for Cassini equates to about half a Titan year. The top panel in Figure 5 shows that the region south of the NS boundary is brighter across all wavelengths except in methane bands, like $0.89 \mu\text{m}$. At equinox, the NS flux ratio increases until the profile has NS flux ratio values greater than 1, indicating a meridional movement of the stratospheric haze layers, vertical motion, and/or differences in aerosol properties. The extent to which changes in the location of the NS boundary are influenced by any one of these factors is unclear, but it is likely that the changes result from multiple factors, each playing a role in the movement of the boundary. The flat T108 NS flux ratio profile near northern summer indicates that the NSA has disappeared at all wavelengths. Then in 2017, we observe a new set of inverted profiles with NS flux ratios over 1 at visible wavelengths of $0.4\text{--}0.75 \mu\text{m}$ and below 1 at infrared wavelengths of $0.8\text{--}1.05 \mu\text{m}$. The profile inversion suggests the formation of a new NS boundary above the equator. Outlier fluctuations in the NS flux ratio with wavelength can be attributed to a wavelength-dependent haze single-scattering albedo and atmospheric gaseous absorption. We observe a gradual increase in the NS flux ratio as time progresses through the flybys with a minimum value of 0.773 at $0.51 \mu\text{m}$ in the Ta flyby (2004), 1.034 at $0.41 \mu\text{m}$ for T67 (2010), and 1.25 at $1.03 \mu\text{m}$ for T108 (2015). As for averages, Ta, T67, and T108 exhibit an average flux ratio of 0.922, 1.17, and 1.29, respectively.

3.3. Implications for Global Circulation

The evolution of the meridional haze brightness profiles over the Cassini mission traces atmospheric circulation at different altitudes in the stratosphere. Insolation, the quantity of solar

radiation received by a certain area, drives Hadley circulation in the upper atmosphere with upwelling at the summer pole and subsidence at the winter pole (Tokano 2007; Lebonnois et al. 2014), driving up haze concentration in the winter hemisphere. The observed reversal in the NS meridional brightness profile before and after the equinox records a clear trend of global Hadley haze circulation driven by seasonal changes in insolation. The NS flux ratio spectra show a similar reversal (across the NS flux ratio value of 1 or the red dashed line in Figure 5) in the methane absorption band profiles over the seasons at visible and infrared wavelengths, sampling altitudes between 60 and 250 km (Robinson et al. 2014). The combination of the meridional profile and NS flux ratio spectra observations over a Titan half year further support the idea of a positive feedback loop between the global atmospheric circulation patterns and haze production (Rannou et al. 2002) where the global movement of the atmosphere, as observed by the changes in the NSA, influences the production of haze. In turn, the haze particles can further exacerbate the magnitude of atmospheric circulation and haze concentration. This synergistic relationship influences both the number of haze particles, but also the seasonal movements of Titan's atmosphere. Our results on the contrasting brightness profiles match well with other recent works analyzing the NSA brightness differences with spectral models (Kutsop et al. 2022) and modeling haze concentrations associated with the NSA using principal component analysis (Karkoschka 2022).

4. NS Boundary

4.1. Boundary Latitude

The straight-line interhemispheric boundary was the most prominent feature in the first high-quality spatially resolved

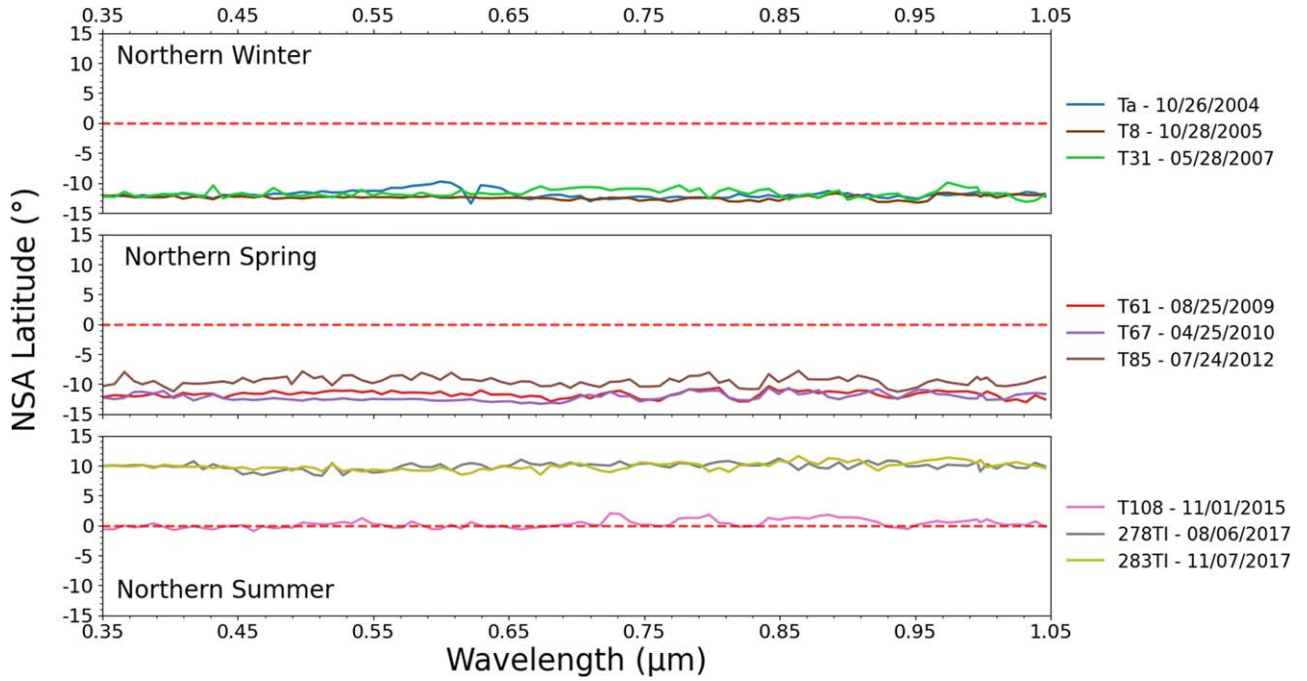


Figure 6. NS boundary latitudes from select flybys that represent a Titan half year. As expected, the data show no evidence of a relationship between wavelength and NS boundary latitude. Even in wavelengths where the NS flux ratio is 1, gradient-based indicators for the NS boundary remain due to the wide sampling latitudinal range ($\pm 30^\circ$).

images of Titan, those taken by the Voyager 1 spacecraft in 1980. The initial examination of those images suggested that the boundary was within 5° of the equator near the northern spring equinox (Smith et al. 1981). The location of the boundary as seen by Voyager 2 nearly a year later was essentially identical: Squyres et al. (1984) determined the latitude of the boundary with some precision in both data sets to be $5.5^\circ \pm 1^\circ$ S. Flasar et al. (1981) observed a strong superrotation of the Titan atmosphere at all latitudes through temperature variations. The slow rotation of Titan makes its superrotating atmosphere more prominent, with the haze changes documented in our study suggesting that the stratosphere exhibits a near-seasonal evolution of circulation patterns. There were no resolved observations of Titan between Voyager 2 in 1981 and 1990 when the new HST imaged Titan. However, the deconvolution of HST images fit with models (Caldwell et al. 1992) suggested that the boundary was located at $32^\circ \pm 10^\circ$ N.

Lorenz et al. (1997) reported that the best fit for postrepair HST images acquired in 1994 and 1995 suggested that the boundary was between 10 and 20° N. Further HST images in 1997 and 2000 were examined by Lorenz et al. (2004)—and although the appearance in each case is not inconsistent with a near-equatorial boundary, the contrast is both weak and takes the form of a ramp rather than a step, so it was difficult to define a precise boundary latitude. During the northern winter from 2002 to 2003, an inspection of NS profiles of $0.435 \mu\text{m}$ HST images by Lorenz et al. (2006) also showed a ramp in albedo ratio (the sharpness of the albedo boundary is in part reduced owing to the telescope point-spread function), but the contrast was then large enough (in a sense opposite from that in the mid-1990s) such that the midpoint of the ramp could define an approximate boundary. The 2002 December image ramp spanned 40° S to 10° S, and so 20° S to 22° S is near the 25° S midpoint; the 2003 image ramp is a little better defined and

spanned 45° S to 0° . The difference in position between 2002 and 2003 did not appear to be significant (although the contrast between hemispheres did increase noticeably). Examination of the 2002 images at $0.502 \mu\text{m}$ and $0.892 \mu\text{m}$ suggests a similar contrast boundary latitude within 5° at those wavelengths. From the Cassini mission, Roman et al. (2009) analyzed ISS images taken from 2004 to 2007 to pin down the clear NSA boundary to $\sim 8^\circ$ S within an error margin of 2° .

Now, we show observations from VIMS cube images taken from flybys acquired over the entire Cassini mission in Figure 7. We adopt a stretch that enhances the visibility of the high-contrasting band for Figure 7 which also tends to accentuate noise and instrument artifacts.

In Figure 6, we observe not only the brevity of the change in latitudes as the seasons progress but also a lack of relation between wavelength and boundary latitude. This static location of the boundary as a function of wavelength suggests an attribution of global circulation rather than truly altitude-dependent processes.

Between the Ta and T92 flybys, we observe the high-contrasting band south of the equator (red dashed line in Figure 7). After T92, the high-contrasting band is not visible in all targeted flyby images (e.g., T108), and instead, multiple bands appear at random locations far from the equator. The extra bands are consistent with observations of secondary bands appearing during the northern summer (Kutsop et al. 2022), but are not the focus of this publication. The NSA boundary latitudes stay at fairly constant values of 8 – 11° S. We only witness the return of the high-contrasting band in two nontargeted flybys 278TI and 283TI, imaging Titan in mid-2017, which owing to spacecraft observation geometry only include half-disk observations just below the equator. However, the high-contrasting band in the 2017 images indicates that the NSA boundary flipped across the equator. The new

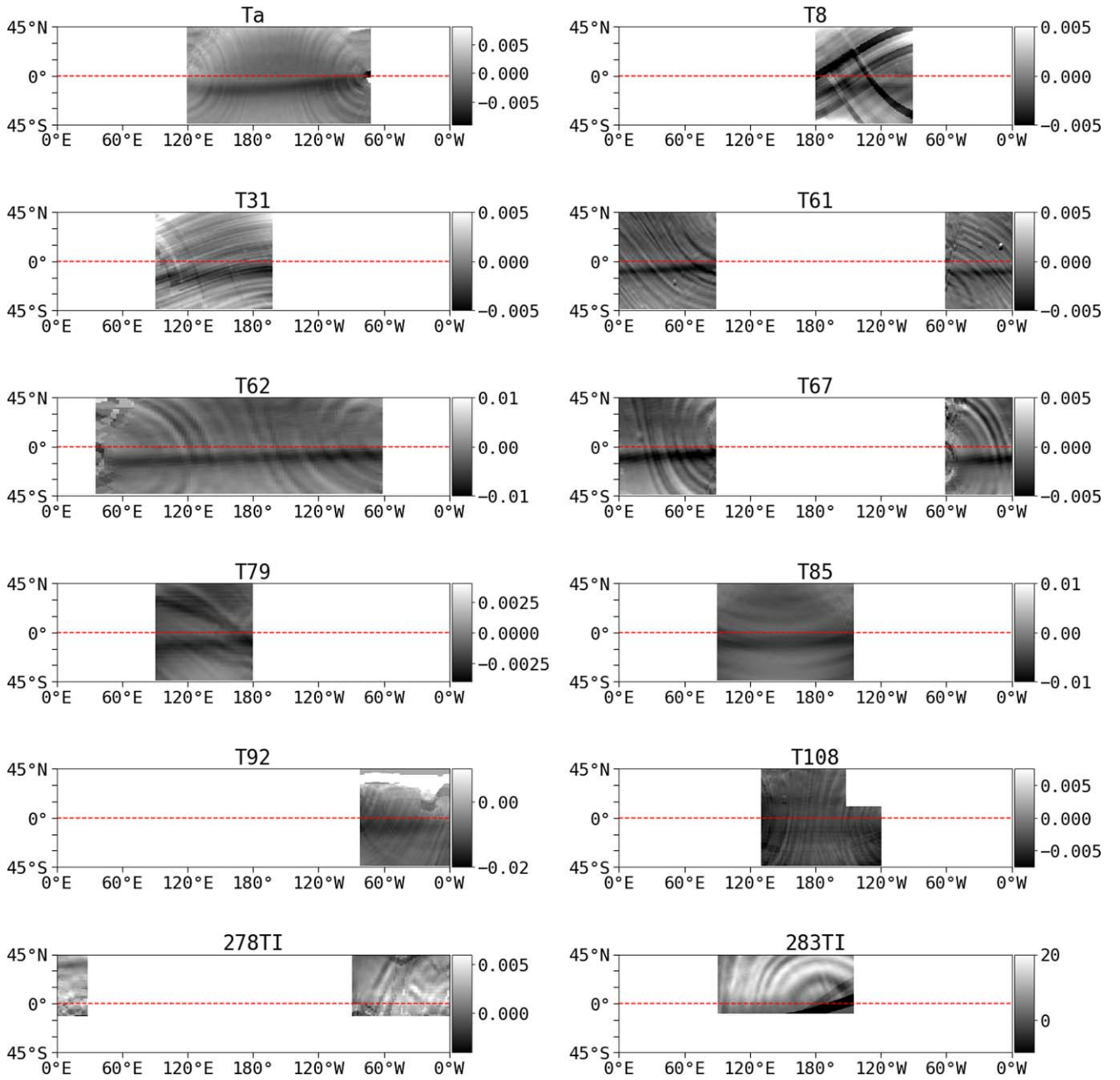


Figure 7. Cylindrical projection maps of the high-contrasting band for every flyby with a faint demarcation of the equator in red. The color bar shows the brightness difference between two vertically shifted images. The dark band is visible in most flybys. We note two distinct bands in the T108 image, which hints at the lack of an NSA boundary.

NSA boundary latitude was approximately 10°N within an error margin of 4° .

4.2. Boundary Tilt

Looking further at the high-contrasting bands in Figure 7, many of the bands appear to be slanted or tilted with respect to the symmetry axis of the bands, indicating an offset in the atmospheric circulation axis relative to the rotational axis of Titan (Achterberg et al. 2008a; Roman et al. 2009; Kutsop et al. 2022). The tilt angle is positive for high-contrasting bands oriented above the geographic equator. Roman et al. (2009) made a similar observation of a tilt in the NSA during the early flybys from 2004 to 2007. Visually speaking, the tilts of the

high-contrasting bands in our VIMS images for select flybys (Ta, T31, and T62) do not appear linear across all longitudes. That is, they remain horizontal on the left side of the band until starting a gradual upward tilt on the right side. Nonetheless, we chose to use the higher-quality VIMS observations from T67 to deduce tilt measurements with a least-squares linear regression, shown in Figure 8. Overall, we find further evidence for a small, detectable tilt of the NSA boundary, despite the lower spatial sampling of the VIMS cube images. Similar measures of the tilt angle between 2° and 6° were found in an analysis of circumpolar bands in VIMS images (Kutsop et al. 2022).

Consequently, we find rough estimates for the tilt angle ranging from 1° to 2° , as opposed to the 4° of Roman et al. (2009). Though the method for deriving tilt is suboptimal given

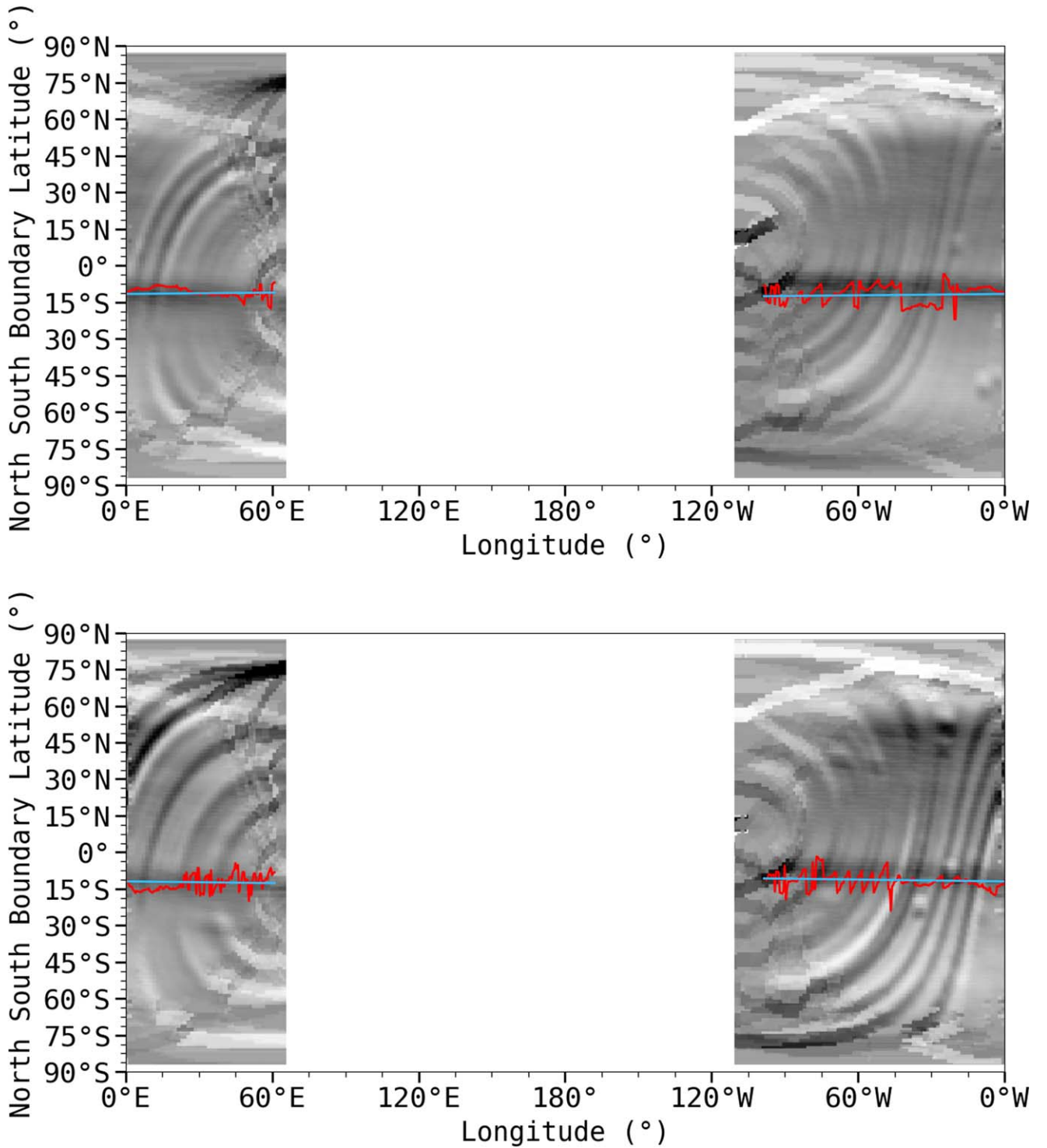


Figure 8. The top and bottom panels show T67 VIMS cube images at 0.886 and 1.003 μm , respectively. These maps show a visible tilt in the NSA boundary. Some mapping artifacts and voids have been removed to show only the parts of Titan visible during the flyby. The red line tracks individual measurements of the NSA boundary latitude for image columns where the NSA is evident. The blue line shows a linear regression model fit to those NSA boundary latitudes to determine a tilt angle for the NSA boundary. The linear fit indicates that at 0.886 μm , the NSA boundary is located $12^\circ\text{S} \pm 3^\circ$ with an angle of $-0.81^\circ \pm 0.22^\circ$. At 1.003 μm , the NSA boundary is at $12^\circ\text{S} \pm 0^\circ$ with an angle of $-0.55^\circ \pm 0.23^\circ$. These fits and their errors assume a linear tilt to the NS boundary, as opposed to a spherical offset of the atmospheric pole from the rotational pole. Therefore the reported measurement precision may underrepresent the true accuracy after accounting for systematic errors due to our underlying tilt assumption.

the changes in observation geometry and the fact that a linear fit is being applied to a projection of Titan rather than the moon itself, the current method provides the best point of comparison to previous works. The reported measurement precision may underestimate the true accuracy of the tilt due to the systematic

differences found in our underlying assumption of a linear tilt, as opposed to a spherical offset of the atmospheric pole. We also note that the tilt angle is only one factor influencing the geometry of the NSA boundary in the Titan images. Other factors include an azimuthal offset from the subsolar longitude

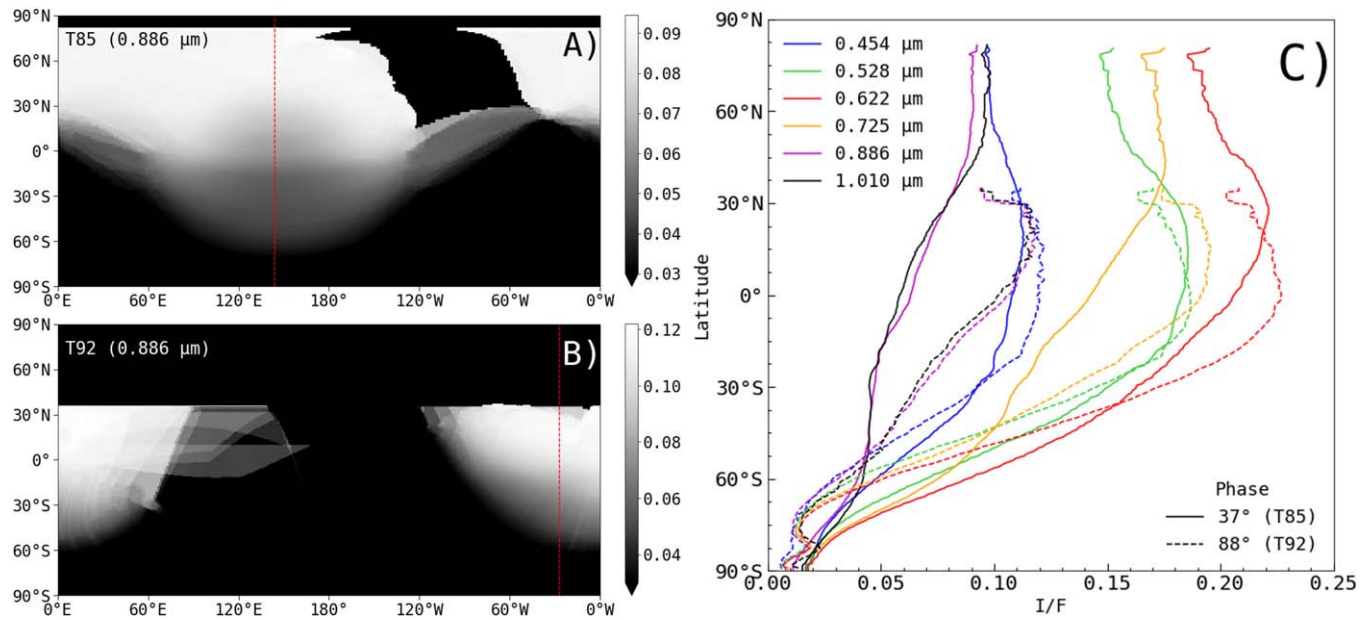


Figure 9. Individual VIMS cube images at 0.886 μm taken within one year of each other at a low (37°) and high (88°) phase angle, respectively. The right plot (C) shows a comparison of the meridional profiles for the two phase angles in several methane windows. At blue and green wavelengths, there is little change between the corresponding low- and high-phase profiles. Differences between the two phases increase at longer wavelengths, while the gradient in I/F vs. latitude becomes more shallow at the longest wavelengths. The red dashed lines in (A) and (B) indicate the longitude of the meridional profiles from each image.

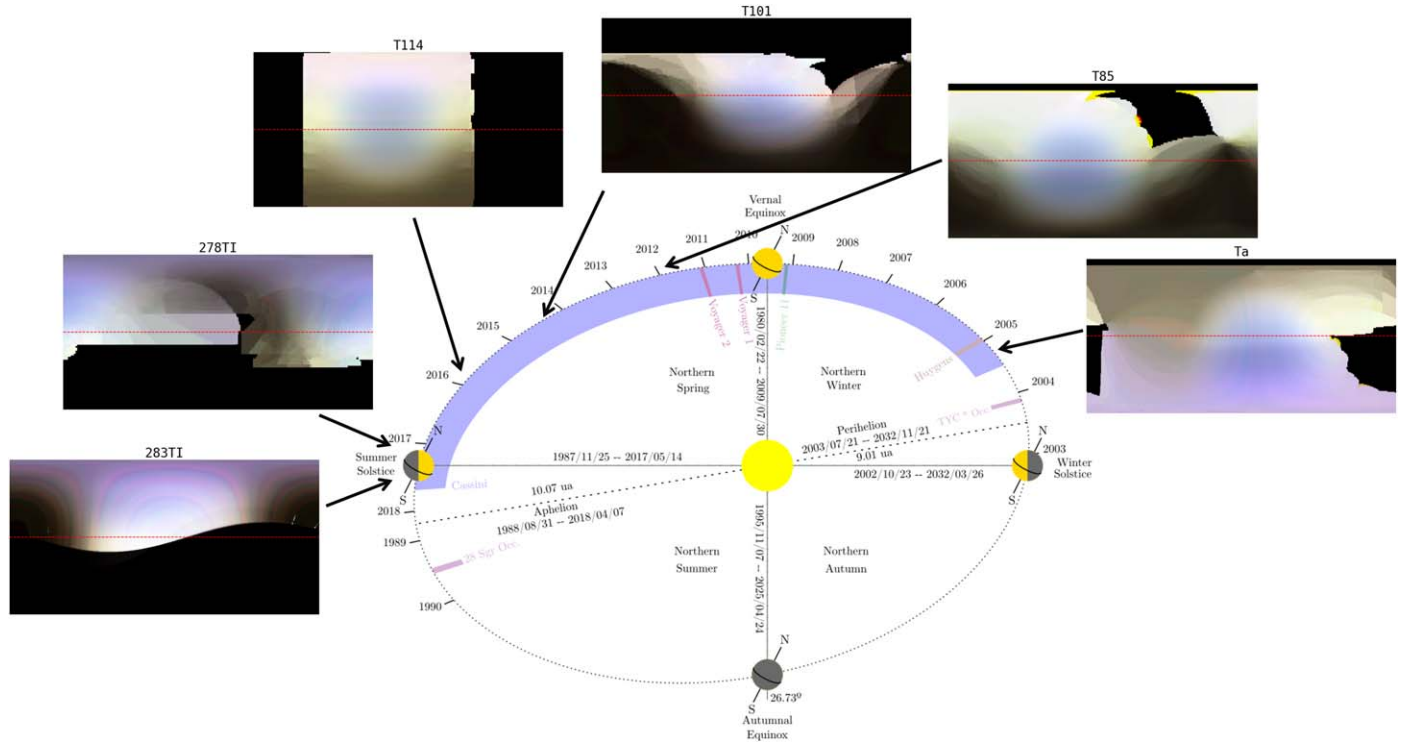


Figure 10. A sequence of false-color (RGB: 0.725, 0.886, 1.003 μm , respectively), near-infrared VIMS cube images show the fading and flipping of the NSA boundary over a Titan half year. The orbital diagram is adapted from Figure 1 of Seignovet et al. (2021) to provide context with the Titan seasons. The red dashed lines indicate the equator. The Ta image has a sharp brightness contrast between the bright (violet) and dark (indigo) hemispheres. The NSA contrast was reduced, but the NSA boundary line was still visible below the equator by 2012 (T85). The NSA boundary line is lost in the T101 image, but some purple color remains. The lack of the NSA persists in the T114 image with a uniform (white) disk brightness profile. The NSA does not return until the near-end of the Cassini mission in mid-2017 in the 278TI and 283TI images. The bright and dark hemispheres have flipped with the subtle boundary line above the equator.

(Roman et al. 2009). The origin of the tilt may arise from an offset between the atmospheric and geographic (solid body) poles (Roman et al. 2009). It is not obvious that the obliquity of 4° observed by Achterberg et al. (2008b) in thermal data and by

Roman et al. (2009) in 0.889 μm images should have been constant throughout the seasonal cycle. Although the tilt angle appears to have remained fixed over 2004–2007 (Roman et al. 2009), we find that the tilt value was similarly persistent over

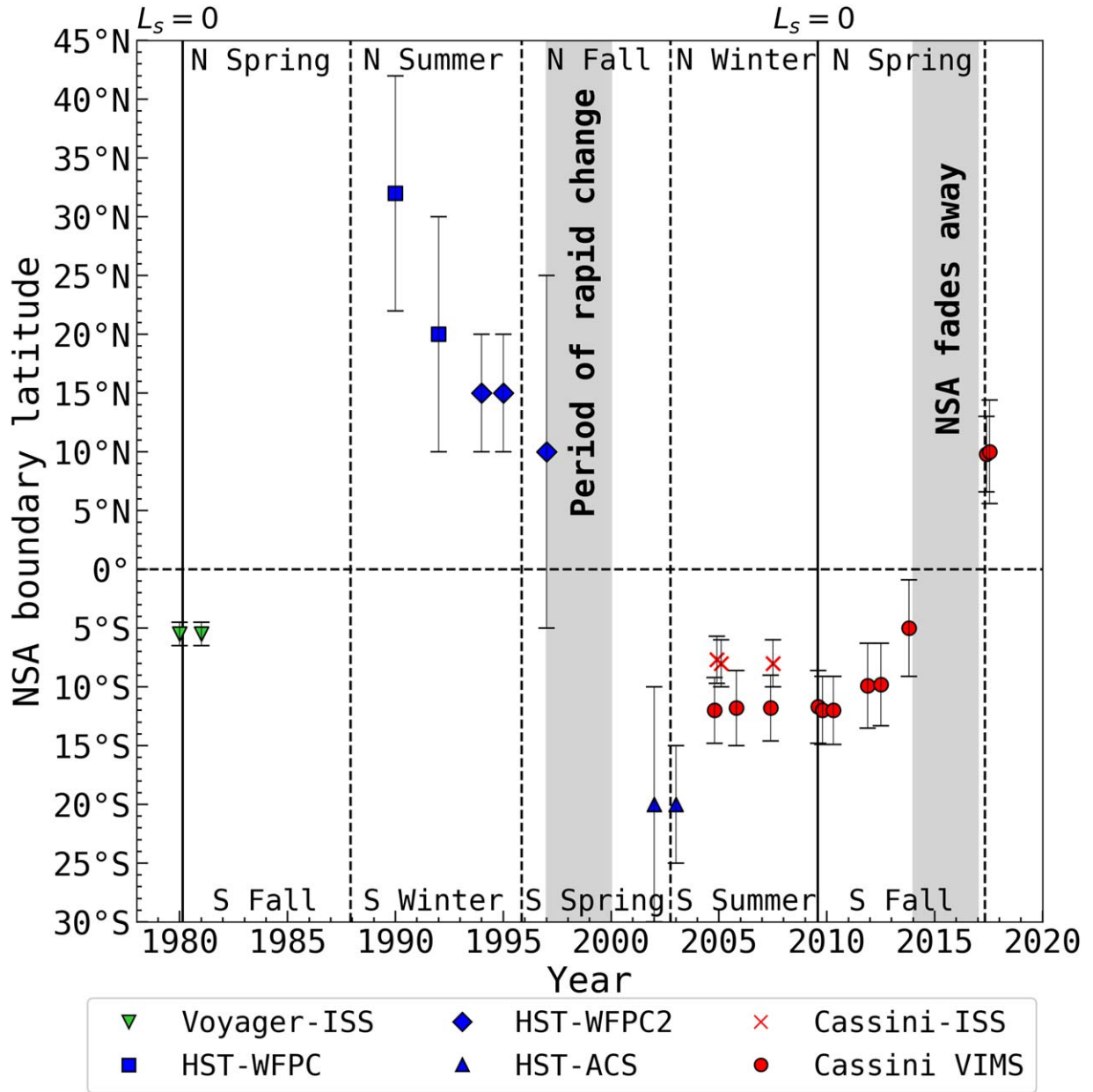


Figure 11. The time line of the NSA boundary latitude as measured by instruments aboard Titan flyby missions and space telescopes. Before 2000, there was more uncertainty in the NSA boundary due to the reliance on noisier HST images. The period of rapid change applies to the early HST observations of seasonal NSA changes reported in Lorenz et al. (2001). Nearly half of Titan’s 29.5 yr seasonal cycle is precisely documented with the new VIMS NSA boundary data set. A period of a stable NSA from 2004 to 2014 was halted by an abrupt change in the fading of the NSA boundary from 2014 until its reversal and reappearance in 2017. Note that small systemic variations within the uncertainties exist in the NSA boundary latitude estimations between the Cassini ISS and VIMS images from 2004 to 2007. L_s refers to solar longitude: 0° at Titan’s northern spring equinox.

the Cassini Mission (2004–2017) even though the boundary does migrate over the course of a year.

4.3. Low versus High Phase

A comparison of NSA images ($0.886 \mu\text{m}$) at a low (37°) and high phase (88°) angles is shown in Figure 9. The images were taken only nine months apart for a minimally biased comparison. We observe that the NSA boundary is still detectable at a high phase angle, albeit at lower contrast. Differences between low and high phase angles are relatively small (less than 0.02 in I/F at boundary latitudes) for the blue- and green-wavelength filters. However, at longer wavelengths, the meridional profiles show more considerable differences

between the two phase angles. The high-phase profiles show a more gradual gradient and more southerly inflection point from 60°S to 30°N relative to the low-phase profiles.

At near-infrared wavelengths, high-phase-angle values exhibit a generally higher I/F. These NSA observations at different phases demonstrate that the haze phase function of the aerosol particles influences the overall brightness of the NS brightness profile, muting the contrast when viewing at higher phase angles. The degree of the reduced contrast varies with wavelength, such that the contrast minimizes within the methane windows at optical wavelengths. In near-infrared methane windows, the phase effect is less pronounced, and the contrast is similar within and outside the windows. Viewing the

NSA at a higher phase angle subdues but does not erase the contrast of the boundary.

4.4. Seasonal Trends

We show the seasonal evolution in the hemispheric profile of the NSA using near-infrared colors in Figure 10. Purple shows the darker hemisphere, while violet and white show the brighter hemisphere with a higher haze concentration (refer to Section 3 for more details). The contrast between the northern and southern hemispheres of the boundary is visible when the boundary is located away from the solid-body equator (red dashed line in Figure 10) during 2004–2013 and 2017 but not when the boundary transitions during 2014–2016. The boundary transitions between the north and south also experience a decrease in contrast as the boundary approaches the equator. Eventually, the brightness contrast between the north and south of the boundary fades away, which marks the start of the transitional period in 2014.

In the T101 and T114 images from Figure 10, the disk shows a uniform white color that indicates the fading of the hemispheric dichotomy. The reemergence of the dichotomy north of the equator does not happen until the latest nontargeted flybys (278TI and 283TI), as noted by the flip in the respective colors of each hemisphere. The VIMS cube images from the nontargeted Titan flybys have poor global coverage and inconsistent striping error that limits the number of usable VIMS cubes.

In our analysis, we document the migration of the NSA boundary during the Cassini Solstice Mission and prior telescope observations in Figure 11. From 2004 to 2010, the boundary remains at a steady 11.8°S , but then experiences a sudden change from 2012 to 2014, where the boundary moves from 9.8°S to 5.0°S . The motion of the NSA boundary in this 2 yr period is also similar to the previous postequinox period from 1995 to 1997 (Lorenz et al. 1999). Over the next 4 yr, the N/S ratio not only reverses but the NSA boundary is observed to be at $\sim 10^\circ\text{N}$, corresponding to a change of $\sim 15^\circ$ (~ 673 km). A similar report of the NSA reversal in an analysis of HST Space Telescope Imaging Spectrograph taken from 1998 to 2004 and 2017 to 2019 (Karkoschka 2016, 2022) corroborates with our finding.

Our new observations resemble the report of a rapid change in the NSA at $0.889\ \mu\text{m}$ between 1997 and 2000 (Lorenz et al. 2001) and confirm the initiation of the NSA reversal across the equator occurs 2–3 yr after the equinox. The VIMS observations constrain the 5 yr transition period into behaviors that are nearly identical to previous NSA observations after the equinox (Sromovsky et al. 1981; Lorenz et al. 1999, 2001). A few years after the equinox, the NSA boundary begins moving toward the equator at a rate of a few degrees of latitude per year for ~ 2 yrs. Afterward, the NSA boundary vanishes, reflecting a more diffuse transition between the hemispheres, where the NSA is viewed as a gradient rather a global phenomena with a localized feature (the NS boundary).

The evolution of the NSA boundary over a Titan year can be broken up into two distinct periods of change. One period includes a constant extrema latitude for several years until the equinox, followed by the second period of rapid linear change, and the distinct NSA fades away until the boundary reappears on the other side of the equator. Seasonal variations in the global atmospheric circulation may vary the NSA latitude for each extremum of the NSA cycle.

5. Conclusion

The NSA in the haze between Titan’s hemispheres tracks the evolution of haze abundances driven by the global atmospheric circulation of Titan. Given the Cassini VIMS data, we can accurately monitor changes in the stratosphere of Titan through a nearly half-year seasonal cycle using consistent instruments and analysis. We find the seasonal changes in the NSA boundary latitude and hemispheric flux dichotomy follow a two-step sequence. A period of constant NSA boundary latitude with a slow changing flux ratio for several years from the start of northern winter in 2004 until a few years after the vernal equinox in 2011. In 2012, a rapid change in the NSA boundary shifted toward the equator and subsequently fades away until reappearing in the opposite hemisphere during northern summer in 2017. The current study also finds a detectable, few degrees tilt of the NSA (-0.8 ± 0.2 and -0.6 ± 0.2 in T67 at $0.886\ \mu\text{m}$ and $1.003\ \mu\text{m}$, respectively) that reinforces the presence of a superrotating atmosphere found in Achterberg et al. (2008a) and Roman et al. (2009), who found tilts of $4^\circ \pm 2^\circ$ and 3.8 ± 0.9 , respectively. We demonstrate that the NSA boundary is detectable at higher phase angles up to 90° with reducing I/F contrast.

Two products from global circulation models (GCMs) would be useful to match with observations such as those described here (and those that might be developed from Earth-based observations in the coming decade).

First are tables of haze abundance versus latitude and altitude at different dates (seasons). These would allow the generation of synthetic images (or profiles of I/F versus latitude) for visible images, and similarly (with an assumed methane profile) for the near-infrared. Since different wavelengths probe different altitude ranges, and it has already been noticed (e.g., Lorenz et al. 1999) that the highest altitudes (e.g., those in the blue, or deep in methane bands) change first, comparison of these data with GCM results would be a valuable constraint to refine the latter. Although there have been useful discussions of GCM predictions of the detached haze layer (which has an optical depth that is small enough to be neglected in the images studied here). The extent to which GCMs with aerosols as tracer particles yield sharp NSA boundaries versus brightness “ramps” has not, to the present authors’ knowledge, been reported.

Second, apart from the detached haze layer (e.g., West et al. 2018), the quantitative association of optical albedo features in Titan’s haze with specific features of the meridional circulation has not been attempted. Specifically, it is tempting to associate the sharp near-equatorial NSA transition observed here and before with the boundary between two symmetric meridional circulations (i.e., Hadley cells) seen in models around equinox (e.g., Figure 4 in Lora et al. 2015). The latter model shows a symmetric (i.e., two-cell) meridional stream function pattern at relevant altitudes (100 km) at $L_s = 180$, but that the pattern has become single cell (pole–pole) by $L_s = 250$. The extent to which the symmetric circulation becomes asymmetric (with the summer cell growing, its downwelling branch progressively encroaching into the winter hemisphere) versus it simply fading away with constant latitude boundaries to be replaced with a progressively intensifying pole–pole mode is not presently clear, but could be elucidated with appropriate model outputs.





In the not-too-distant future, missions such as the Dragonfly drone or an orbiter (Lorenz et al. 2018; Barnes et al. 2021) could lead to an active probe that can measure in situ changes in the lower atmosphere on a more localized level instead of

through changes in haze observed from orbit. Future analysis can examine the long-term effects of a superrotating atmosphere on Titan, and data taken over a larger period of time can aim to gain a better understanding of the movement of the atmosphere relative to the rotational axis. In addition, a study analyzing the correlation between the polar hood and the seasonal motion of the NSA boundary could reveal new details about the haze distributions.

Acknowledgments

A.V. is supported by the Dyess Fellowship at the University of Idaho. M.F.H. and J.W.B. are supported by NASA Cassini Data Analysis Program grant 80NSSC19K0896. C.H. was supported by the NASA/ESA Cassini project.

ORCID iDs

Aadvik S. Vashist  <https://orcid.org/0000-0002-6318-7226>
 Michael F. Heslar  <https://orcid.org/0000-0002-9304-8657>
 Jason W. Barnes  <https://orcid.org/0000-0002-7755-3530>
 Ralph D. Lorenz  <https://orcid.org/0000-0001-8528-4644>

References

- Achterberg, R., Conrath, B., Gierasch, P., Flasar, F., & Nixon, C. 2008a, *Icar*, **197**, 549
- Achterberg, R. K., Conrath, B. J., Gierasch, P. J., Flasar, F. M., & Nixon, C. A. 2008b, *Icar*, **194**, 263
- Barnes, J. W., Turtle, E. P., Trainer, M. G., et al. 2021, *PSJ*, **2**, 130
- Brown, R. H., Baines, K. H., Bellucci, G., et al. 2004, *SSRv*, **115**, 111
- Brown, R. H., Lebreton, J.-P., & Waite, J. H. 2009, Titan from Cassini-Huygens (Berlin: Springer)
- Caldwell, J., Cunningham, C. C., Anthony, D., et al. 1992, *Icar*, **97**, 1
- Flasar, F., Samuelson, R., & Conrath, B. 1981, *Natur*, **292**, 693
- Hirtzig, M., Coustenis, A., Gendron, E., et al. 2006, *A&A*, **456**, 761
- Karkoschka, E. 2016, *Icar*, **270**, 339
- Karkoschka, E. 2022, *Icar*, **387**, 115188
- Kutsop, N., Hayes, A., Corlies, P., et al. 2022, *PSJ*, **3**, 114
- Lebonnois, S., Flasar, F. M., Tokano, T., & Newman, C. 2014, in Titan, ed. I. Müller-Wodarg (Cambridge: Cambridge Univ. Press), 122
- Lora, J. M., Lunine, J. I., & Russell, J. L. 2015, *Icar*, **250**, 516
- Lorenz, R., Young, E., & Lemmon, M. 2001, *GeoRL*, **28**, 4453
- Lorenz, R. D., Lemmon, M. T., & Smith, P. H. 2006, *MNRAS*, **369**, 1683
- Lorenz, R. D., Lemmon, M. T., Smith, P. H., & Lockwood, G. 1999, *Icar*, **142**, 391
- Lorenz, R. D., Smith, P. H., Lemmon, M. T., et al. 1997, *Icar*, **127**, 173
- Lorenz, R. D., Smith, P. H., & Lemmon, M. T. 2004, *GeoRL*, **31**, L10702
- Lorenz, R. D., Turtle, E. P., Barnes, J. W., et al. 2018, *JHATD*, **34**, 14
- Rannou, P., Hourdin, F., & McKay, C. 2002, *Natur*, **418**, 853
- Robinson, T. D., Maltagliati, L., Marley, M. S., & Fortney, J. J. 2014, *PNAS*, **111**, 9042
- Roman, M. T., West, R. A., Banfield, D., et al. 2009, *Icar*, **203**, 242
- Seignovert, B., Rannou, P., West, R. A., & Vinatier, S. 2021, *ApJ*, **907**, 36
- Smith, B. A., Soderblom, L., Batson, R., et al. 1982, *Sci*, **215**, 504
- Smith, B. A., Soderblom, L., Beebe, R., et al. 1981, *Sci*, **212**, 163
- Smith, P., Karkoschka, E., & Lemmon, M. 1992, *BAAS*, **24**, 950
- Squyres, S., Thompson, W., & Sagan, C. 1984, *BAAS*, **16**, 664
- Sromovsky, L. A., Suomi, V. E., Pollack, J. B., et al. 1981, *Natur*, **292**, 698
- Tokano, T. 2007, *P&SS*, **55**, 1990
- Tomasko, M. G., Archinal, B., Becker, T., et al. 2005, *Natur*, **438**, 765
- Vixie, G., Barnes, J. W., Bow, J., et al. 2012, *P&SS*, **60**, 52
- West, R. A., Balloch, J., Dumont, P., et al. 2011, *GeoRL*, **38**, L06204
- West, R. A., Seignovert, B., Rannou, P., et al. 2018, *NatAs*, **2**, 495